

Single vacancy defect in graphene: Insights into its magnetic properties from theoretical modeling

A. M. Valencia* and M. J. Caldas

Instituto de Física, Universidade de São Paulo, CEP 66318, 05315-970, São Paulo, São Paulo, Brazil

(Received 24 November 2016; revised manuscript received 28 July 2017; published 21 September 2017)

Magnetic properties of a single vacancy in graphene is a relevant and still much discussed problem. The experimental results point to a clearly detectable magnetic defect state at the Fermi energy, while calculations based on density functional theory (DFT) yield widely varying results for the magnetic moment, in the range of $\mu = 1.04\text{--}2.0 \mu_B$. We present a multitool *ab initio* theoretical study of the same defect, using two simulation protocols for a defect in a crystal (cluster and periodic boundary conditions) and different DFT functionals—bare and hybrid DFT, mixing a fraction of the Hartree-Fock (HF) exchange. We find that due to the π character of the Fermi-energy states of graphene, delocalized in the in-plane and localized in the out-of-plane direction, the inclusion of the HF exchange is crucial, and moreover, that defect-defect interactions are long-range and have to be carefully taken into account. Our main conclusions are two-fold. First, for a single isolated vacancy we can predict an integer magnetic moment $\mu = 2\mu_B$. Second, we find that due to the specific symmetry of the graphene lattice, periodic arrays of single vacancies may provide interesting diffuse spin-spin interactions.

DOI: [10.1103/PhysRevB.96.125431](https://doi.org/10.1103/PhysRevB.96.125431)**I. INTRODUCTION**

A single vacancy is the simplest intrinsic defect in a crystal, and has been seen in graphene with atomic resolution through transmission electron microscopy (TEM) [1,2] and scanning tunneling microscopy (STM) [3]. When the atom is removed, two scenarios are possible: either the disrupted bonds remain as dangling bonds or the structure undergoes a bond reconstruction through a Jahn-Teller rearrangement, and in three-dimensional (3D) semiconductors we find a localized state and deep gap levels. Graphene, on the other hand, has notable two-dimensional (2D) properties with the covalent bonding introducing two intrinsically different state types, σ and π , these last relevant for the Fermi-energy and Dirac point properties. The π states are diffuse in the 2D planar (x, y) directions, but very localized on the z direction with an in-plane node. As such, long-range 2D electron-electron interaction is enhanced. In addition, the hexagonal structure with two sublattices creates for the π states the special band structure with the Dirac point. We might thus expect special properties also for the vacancy in graphene. There is controversy from the experimental side about the reconstruction [4,5], however, a clear symmetry is found for the defect, and in particular, from scanning tunneling microscopy [3,5] it is found also that the defect level is resonant at the Dirac point, and induces magnetism [5].

A number of theoretical studies of the electronic and magnetic properties of the vacancy in graphene were reported in the past decade [5–18]. In particular, first-principles calculations based on density functional theory (DFT) [5,8–17] yielded widely varying results for the magnetic moment, in the range of $1.04\text{--}2.0 \mu_B$. For instance, Palacios and Ynduráin [12] found that the magnetization decreases with decreasing defect density, tending to $1.0 \mu_B$ in the low-density limit. On the other hand, Yazyev and Helm [11] reported that the magnetization increases from 1.15 to $1.5 \mu_B$ with decreasing density.

These results highlight the possibility of magnetic moment dependence with defect-defect interaction.

Regarding this last point, two typical approaches can be used for the simulation: model clusters, which are assumed to resemble the defect environment in the bulk, or periodic boundary conditions based on the choice of *supercells* (SC). In the cluster model we must be careful about defect interaction with cluster edge states, which in the case of graphene can be critical [19,20]. As for the SC modeling, we must remember that we will study defects periodically arranged [21], that is, we study an *array of defects* that may induce spurious defect interactions.

Concerning the defect-edge interactions and focusing on the π states, when we have flakes with zig-zag edges we can (depending on the flake symmetry) bring in Lieb's imbalance states [22] that will group at the Fermi energy. These states are not realistic concerning the modeling of infinite graphene (no Lieb's imbalance), so we should not adopt such flakes for use as clusters. In the case of SCs we have for graphene three different symmetrical ($N \times N$) families, as shown in Refs. [23,24], namely $(3n \times 3n)$, $(3n - 1 \times 3n - 1)$ and $(3n + 1 \times 3n + 1)$, where n is an integer number. For the $3n$ family, there occurs a folding of the $K - K'$ points onto the Γ point of the SC Brillouin zone, that is, we will have degenerate, fully delocalized π -character states of different original symmetry crossing the Fermi energy at the SC Γ point. These delocalized states show strong interference with localized defect states, through the long-range interaction property of the Γ point, which is softened when we adopt either one of the other families. Still for supercells, due to the π symmetry of the relevant states at the Fermi region, we also have to take into account the possibility of long-range interaction between defects coming from parity in the zig-zag direction, as will be seen here.

In this work we adopt both the cluster approach, choosing hexagonal clusters with arm-chair and zig-zag edges, and periodic conditions with symmetrical cells from the different families $(3n \times 3n)(6 \times 6)$, $(3n + 1 \times 3n + 1)(7 \times 7)$, and $(3n - 1 \times 3n - 1)(8 \times 8)$, as also a different symmetry cell (6×9) . We use semilocal DFT [25] and hybrid DFT including

*valencia@if.usp.br

a fraction α of Hartree-Fock exchange XC [26], in which α is chosen to reproduce the properties of perfect graphene in the Fermi energy region [27].

We remark that, for the dimensions of supercells we adopt, we see always defect-defect interaction, while for the clusters we use there is still a sizable confinement effect. However, we can extract from our results that the isolated vacancy defect introduces a magnetic moment of $2\mu_B$. It is critical to include a proper fraction of XC to arrive at a coherent description. Moreover, we find that periodic arrays of the defect can bring in interesting long-range spin dispersion effects [28,29].

II. METHODOLOGY

The calculations in this work are performed using the all-electron Fritz Haber Institute *ab initio* molecular simulations code (FHI-aims) [30], with or without spin-polarization: the code employs numeric atomic orbitals obtained from *ab initio* all-electron calculations for isolated atoms, and can be used at the mean-field level with finite or infinite periodic models. The use of an all-electron code allows us to align the level structure of different simulation models by the deep $1s^2$ C orbitals. For dispersion interactions we adopt the Tkatchenko-Scheffler [31] model, which is sensitive to the chemical bonding environment. We employ *tight* integration grids and TIER2 basis sets [32], and the atom positions are relaxed until the Hellmann-Feynman forces are smaller than 10^{-3} eV/Å. For periodic cells, we use the Monkhorst-Pack [33] (Γ -point included) scheme for sampling the Brillouin zone, with a $[6 \times 6 \times 1]$ grid. The Gaussian smearing is 0.01 eV for all calculations.

We compute the formation energy of the defect and electronic and magnetic properties. The geometry optimization calculations are done using the Perdew-Burke-Ernzerhof (PBE) functional. The formation energy of a vacancy E_F^V is calculated as

$$E_F^V = E(C_{n-1}H_m) + E(\text{carbon}) - E(C_nH_m), \quad (1)$$

where here $E(C_nH_m)$ is the total energy of the perfect cluster, $E(\text{carbon})$ is the average energy of a single carbon atom in graphene, and $E(C_{n-1}H_m)$ the total energy for the relaxed defect cluster. A similar computation is used in the case of periodic conditions.

Standard DFT, with exchange-correlation functionals in the local approximation or semilocal generalized gradient approximation (GGA), is known to suffer from self-interaction errors (SIE) [34] leading to excessive delocalization of electrons [35]. Hybrid density functionals reduce the SIE by mixing in a fraction of Hartree-Fock (HF) exchange and can significantly improve the study of many electronic properties. Now most previous DFT calculations for the vacancy in graphene were performed in the generalized gradient approximation. Since removing a C atom modifies the delocalized π states into a localized defect state, a relevant improvement to the calculations could be the use of hybrid-DFT, since hybrid functionals may describe localized states better than GGA functionals [27]. The general form of the hybrid functional we use is

$$E_x^{\text{PBEh}} + E_c^{\text{PBEh}} = \alpha E_x^{\text{HF}} + (1 - \alpha)E_x^{\text{PBE}} + E_c^{\text{PBE}}, \quad (2)$$

where E_x^{PBE} and E_c^{PBE} denote the PBE exchange and correlation energy, respectively, and E_x^{HF} is the exact HF exchange energy: for example, $\alpha = 0$ corresponds to the PBE, and $\alpha = 0.25$ to the PBE0 functional [36].

The choice of the optimal α factor is system dependent, as shown in Ref. [27]. There, the choice is based on Koopmans theorem for the ionization potential, gauged through many-body G_0W_0 calculations for finite systems. Here we simulate defects in graphene, and as such the goal is to find the optimal factor for the infinite extended system. We cannot apply the same procedure here since we need GW results for the extended crystal, which cannot be obtained with the same code. We rely on theoretical results from the literature for the Fermi velocity v_F , coming from GW methodology [37,38], and experimental results [39] for the Work Function E_W . With this rationale we choose $\alpha = 0.25$, from the much-adopted functional PBE0, with which we obtain $v_F = 1.3 \times 10^6$ m/s and $E_W = 4.35$ eV (compared to $v_F = 0.98 \times 10^6$ m/s and $E_W = 4.24$ eV with PBE).

Regarding the cluster simulation models, the $\sigma - \pi$ character allows us to use hydrogen-saturation of a graphene cut or nanoflake, with the required absence of imbalance states. We adopt for the electronic structure the same factor $\alpha = 0.25$ since we are simulating by the cluster model the defect in the infinite crystal (it must be noted that the optimal factor [27] for this size of nanoflakes would be in the range $\alpha \sim 0.4-0.6$).

Simulations models

It is possible to cut bulk graphene in different sizes and shapes, which allows us to create a cluster model which reproduces some relevant properties for the defect, such as symmetry. Graphene is a particular case for this approximation since nanoflakes can be specifically associated to chemically stable, well-known polyaromatic hydrocarbons (PAHs) [40], and long flakes approach the well-studied graphene nanoribbons [41,42]. In this last case, it is also well known that the character of the saturated border, arm-chair or zigzag, is very important for the electronic structure [43,44]. We here will require that the structural conformation of the perfect cluster involves at least a C_3 symmetry operation, matching the C_3 rotation axis for regular graphene. Two series of hexagonal (H) clusters (D_{6h} group) were analyzed, with arm-chair (AC) and zig-zag (ZZ) edges as shown in Fig. 1 for (HAC)- $C_{222}H_{42}$ and (HZZ)- $C_{216}H_{36}$.

For the specific settings reported above, the resulting average carbon-carbon bond distances are 1.42 Å, and 1.09 Å for carbon-hydrogen bond lengths, and the (C-C-C) angle is 120° , thus we obtained the expected sp^2 hybridization character of carbon atoms. It is important to note that all structures were fully relaxed without any symmetry restriction. All structures remain completely flat after the relaxation of atomic positions, regardless of the size, and the overall symmetry is maintained.

To begin, we show in Fig. 2 the energy spectra for the two clusters, which have a similar number of atoms, $N \sim 220$, but different edges. The highest occupied molecular orbital (HOMO) and the lowest unoccupied molecular orbital (LUMO) are two-fold degenerate for both HZZ and HAC. Already at the PBE level we have a sizable HOMO-LUMO

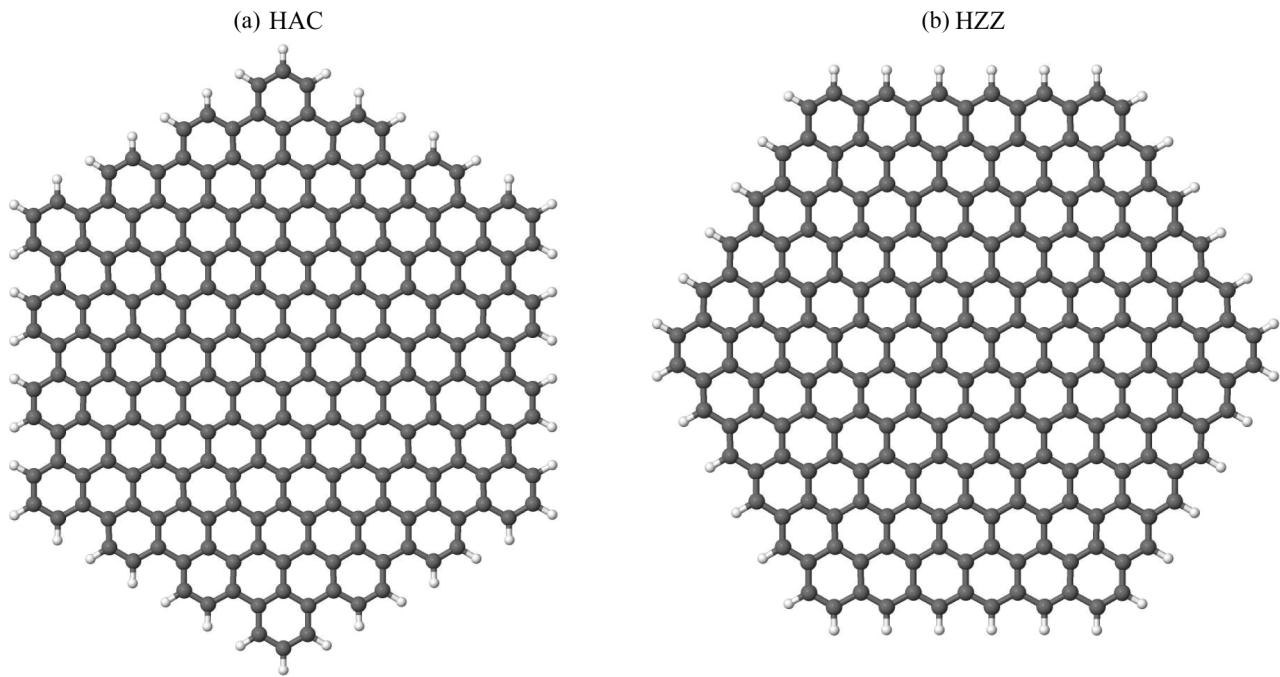


FIG. 1. Cluster models adopted here for graphene, hexagonal D_{6h} symmetry (a) HAC $C_{222}H_{42}$ arm-chair and (b) HZZ $C_{216}H_{36}$ zig-zag edges.

gap coming from the confinement effect, however, it is worth noting that a quite significant increase is seen when we adopt PBE0.¹ As is well known [45,46] this significant increase in the HOMO-LUMO gap is seen for finite systems when a fraction of the exact exchange is included via the hybrid functional approach; here these HOMO-LUMO gaps do not represent the actual gaps expected for nanoflakes due to our choice of α factor, but just the cluster confinement effect. We simulated smaller clusters (HAC from 114 C atoms and HZZ from 96 C atoms) and we see that the HOMO-LUMO gap closure is very slow with the cluster radius, as expected. An important characteristic of the frontier states in the case of zigzag edges is the concentration at the edges, not seen for the armchair cluster; however, we can see that at the center, where the vacancy will be simulated, this effect should not be important. The difference in aromaticity between the clusters also brings a difference in the conjugation design of the frontier states, however, both are fully conjugated.

As reported in the literature in two independent and almost simultaneous papers [19,20], graphene nanostructures can have nonzero spin magnetic moment due to the sublattice imbalance mentioned above (Lieb's theorem) [22]. In the case of hexagonal clusters the sublattice imbalance does not exist so the spin should be zero regardless of the type of edges. Indeed, we verify that none of the states show spin splitting for both PBE and PBE0 functionals. Our results herein are in agreement with earlier theoretical results [19,20,47].

¹For the largest HAC cluster and for the (6×9) and (8×8) supercells using PBE0 we adopt TIER2 with exclusion only of the $H(3d)$ basis; A $H(3d)$ basis is anyhow included in the TIER1 portion of the basis.

Regarding the supercell (SC) models, as said above we will simulate the vacancy in the symmetrical $3n$ (6×6) SC, much adopted in the relevant literature, however, we will compare results to the $3n + 1$ (7×7) and $3n - 1$ (8×8) SCs, which do not carry the same symmetry problems, and also for the nonsymmetric (6×9) SC.

III. VACANCY IN GRAPHENE

Perfect graphene is nonmagnetic, but the presence of the vacancy can induce magnetism, by breaking the symmetry of the π -electron system. Theoretical results are, however, not identical, and depend on the specific model or methodology adopted. As already commented in the Introduction, in the past years several works were dedicated to this study, using the different approaches of cluster or periodic conditions, and different theoretical formalisms [5–17,48,49]. Discussing first the results for the geometrical structure, there is consensus about the occurrence of Jahn-Teller distortion [50] for the surrounding atoms, with two of the three (here named C1 and C2, see Fig. 3) reconstructing, and realizing a (weak) complete σ - π bond, while the remaining (C3) atom carries the σ and π dangling bonds. Also, some of these previous studies [9,10,13,17] found that when the calculation is performed without spin polarization (or with constrained zero spin), the C3 atom is projected out-plane, but when the spin is included (or free) the defect is back to full planar morphology. This is, however not consensual, and indeed the two conformations are very close in energy [13,17,51].

This discussion leads us to reported results for the magnetic moment of the defect, as obtained [9–13,15,17,48,49] from different works: Lehtinen *et al.* [9] and Ma *et al.* [10] reported a magnetic moment of $\sim 1.04 \mu_B$ (8×8 supercell, $3n - 1$ family, PBE-sp). Palacios and Ynduráin [12] detailed the

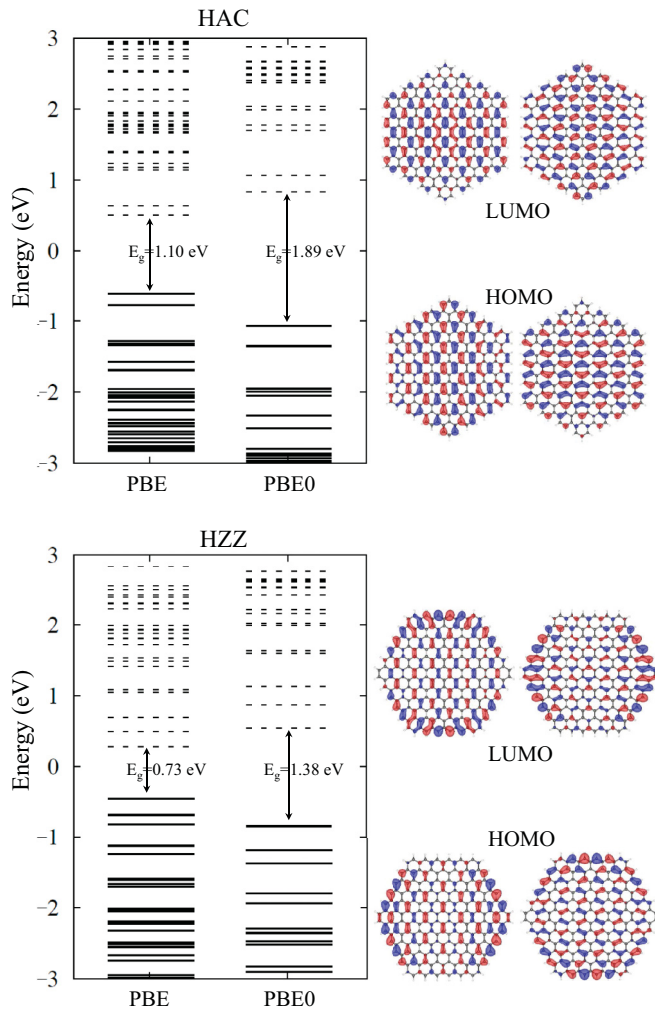


FIG. 2. Electronic energy levels for hexagonal H clusters in the region near the Fermi level, results from PBE and PBE0. Solid (dotted) lines indicate occupied (unoccupied) states. Upper panel HAC- $C_{222}H_{42}$ and lower panel HZZ- $C_{216}H_{36}$. Energies aligned to the Fermi energy of the perfect crystal by the $C-1s^2$ average energy. Isosurfaces for the molecular orbitals (HOMO and LUMO) at the frontier energies from the PBE0 calculations.

analysis, and related the magnetic moment of the vacancy with the size of used supercells ($3n$ family); they found, using PBE-sp, already a magnetic moment of $\sim 1.7 \mu_B$ in a 6×6 supercell, but this value *decreases* to $\sim 1.0 \mu_B$ as the supercell size increases (15×15). Casartelli *et al.* [13] found a maximum of $\sim 1.9 \mu_B$ in a 5×5 supercell, a value that stabilizes $\sim 1.5 \mu_B$ for larger supercells already from 6×6 , up to 10×10 . In an earlier work (all three families, 4×4 to 12×12 supercells, PBE-sp), Yazyev and Helm [11] calculated, however, an *increase* in the magnetic moment, from 1.12 to $1.53 \mu_B$, when the distance between vacancies increases. We see that in all cases where the band structure is reported with details, and as we will see below, the noninteger value of the magnetic moment comes from the crossing of delocalized bending bands at the Fermi energy, giving the system a “doped” character (which, however, is generated by a vacancy, a defect usually associated with a deep-level character

in semiconductors). At the same time, these delocalized bands tell us that the interaction between defects in our supercell models may bring misleading effects.

At introducing a vacancy in supercell or cluster models, we find that it exhibits a *planar* Jahn-Teller distortion, and the point-group symmetry becomes C_{2v} . The reconstruction seen in Refs. [9–12,15,17,48,49] is recovered here, with two of the three affected carbon atoms binding to each other, and one single carbon with dangling bonds remains. The formation energy from PBE-sp results is approximately 7.6 eV, in agreement with earlier theoretical results [8,14,52–54].

We show next our results² for the symmetric supercell models, for which the band structures are shown in Fig. 4. We see first that in all cases we also find noninteger magnetic moments $\mu_V = 1.49\mu_B$ for the (6×6), $\mu_V = 1.30\mu_B$ for the (7×7), and $\mu_V = 1.38\mu_B$ for the (8×8) supercell, coming from the crossing of the bands at the Fermi energy. It is interesting now to look into the details of the band structure for the different supercells. While for the disruption of the σ states we see quite localized defect states (flat bands) which we will call $V\sigma$, with a sizable spin-splitting (~ 2 eV) in all models, the effect on the π electrons is qualitatively different when moving from the $3n$ to the $3n \pm 1$ supercells. Starting with the (6×6) SC we can see that the Dirac point degenerate bands (now upshifted relative to the Fermi energy) show very different behavior. The lower energy band that we call here $d\pi$ shows a clean crossing with the other bands, down to the M_{6SC} folding point, with no interaction except in the Γ_{6SC} - K_{6SC} path very close to the K_{6SC} region; these $d\pi$ up- and down-spin bands are degenerate, so do not add to the total spin. On the other hand, for the $d'\pi$ band, responsible for the total spin and seen in previous works [12,13,15–17], we see a strong anticrossing with the vacancy-related band, which in this case we call $l\pi$ (see Fig. 5), highlighting the defect-defect interaction. This interaction results in a different character for the band eigenstates along the Brillouin zone, so that close to the Γ_{6SC} point the states are highly delocalized (also shown in Fig. 5), down to the Fermi-level crossing points, while at the center of the M_{6SC} - K_{6SC} tract they exhibit localized defect-state character; furthermore, the Fermi-level crossing states show a slightly different character, with the down-spin state presenting a more localized, defect-state character, but with the up-spin state being delocalized, resulting in a spread-out character, with impact on the spin-density.³ The vacancy-related $l\pi$ states

²From nonspin PBE results we observe that after optimization of atomic positions, the vacancy is reconstructed with a weak C1-C2 covalent bond (2.1 \AA) and the C3 is displaced out of the plane by $\sim 0.5 \text{ \AA}$. Also we see that the surrounding atoms are displaced below the plane by 0.2 \AA , resulting in a local rippling, similar to previously reported theoretical results [10,16,52,54,56]. Moving to results from PBE with spin polarization, after the relaxation defective graphene is completely flat. Here the spin-polarized flat structure is more stable by 0.07 eV

³We performed further calculations using the QUANTUM ESPRESSO code [57] that allow us to picture also the non- Γ -point eigenstate densities, and we find that the description of the localized-delocalized character of the states agrees with the conclusions coming from the band-anticrossing analysis.

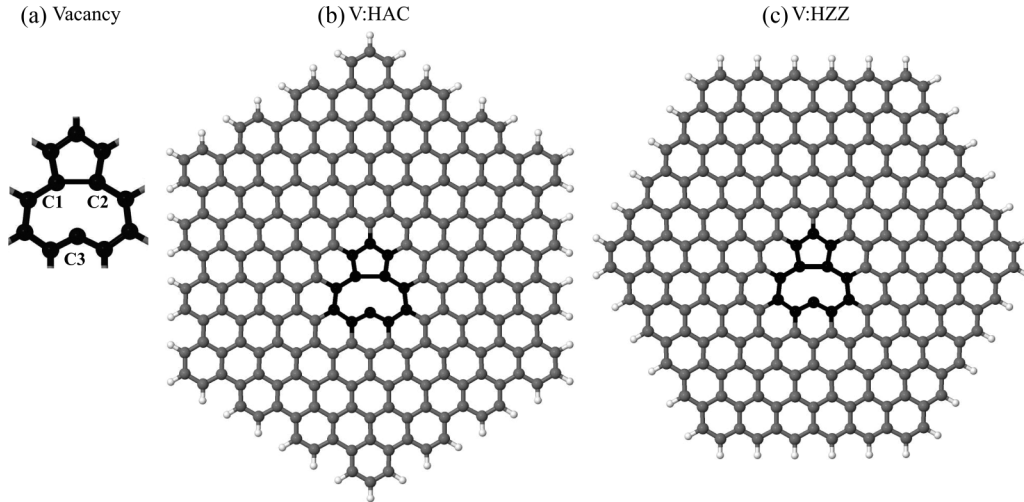


FIG. 3. Vacancy in graphene (a) visualization of the atoms in the close vicinity. Model clusters: fully optimized structures with spin-polarized PBE (b) VHAC- $C_{222}H_{42}$, (c) VHZZ- $C_{216}H_{36}$. All structures remain flat after the structural relaxation.

are in this case affected first by the symmetry-folding and further by the parity of the supercell, interacting through the zig-zag connection. Looking now at our results for the (7×7) SC, free from the parity connection problems, the defect-defect interaction and related band-anticrossing is also seen. We can follow the delocalized bands $d'\pi$ from the Γ_{7SC} point, at $\sim E_f - 1.2$ eV, up to the K_{7SC} at $\sim E_f + 0.4$ eV, while the defect-related bands which we will call $V\pi$, seen at the Γ_{7SC} -point at $\sim E_f - 0.15$, cross the Fermi-level between the Γ_{7SC} and M_{7SC} , but are found at $\sim E_f - 0.3$ eV close to the K_{7SC} point. In this SC delocalized bands are not involved anymore in the spin generation since the Fermi-level crossing band $V\pi$ is the one causing the final (noninteger) magnetic moment. Similar effects are still visible in the (8×8) SC, that is, we also have no symmetry-folding thus the $V\pi$ state is the one crossing the Fermi energy, however, we have parity connection and the $l\pi$ states can also contribute to the final magnetic moment. Moving to the nonsymmetrical (6×9) SC, we still have symmetry folding to the Γ point, the results present the same character found for the (6×6) , and a magnetic moment

of $\mu_V = 1.40\mu_B$. In summary, the defect-related states in these supercells show not only a different total magnetic moment, but also different μ_V characters, and one cannot correlate the variations of μ_V to simple defect-defect distance since these symmetry-related effects are very relevant.

We turn thus to our results using the cluster models. Figure 3 shows the geometric structures of the vacancy in the different clusters, optimized with PBE and spin polarization. The cluster symmetry is broken, from D_{6h} to C_{2v} . The removal of one π orbital creates a lattice imbalance in the hexagonal clusters, with a direct effect on the magnetization. As was reported in Refs. [19,20] perfect clusters with sublattice imbalance have nonzero spin magnetic moments, in accordance to Lieb's theorem. Considering this "counting rules," the magnetic moment of the vacancy in graphene is predicted to be $1\mu_B$. However, one has to keep in mind that Lieb's theorem refers only to π orbitals and the contribution from the σ -dangling orbital is not considered.

We here obtain a magnetic moment of $2\mu_B$ already using PBE-sp in agreement with Wang and Pantelides [49]. This

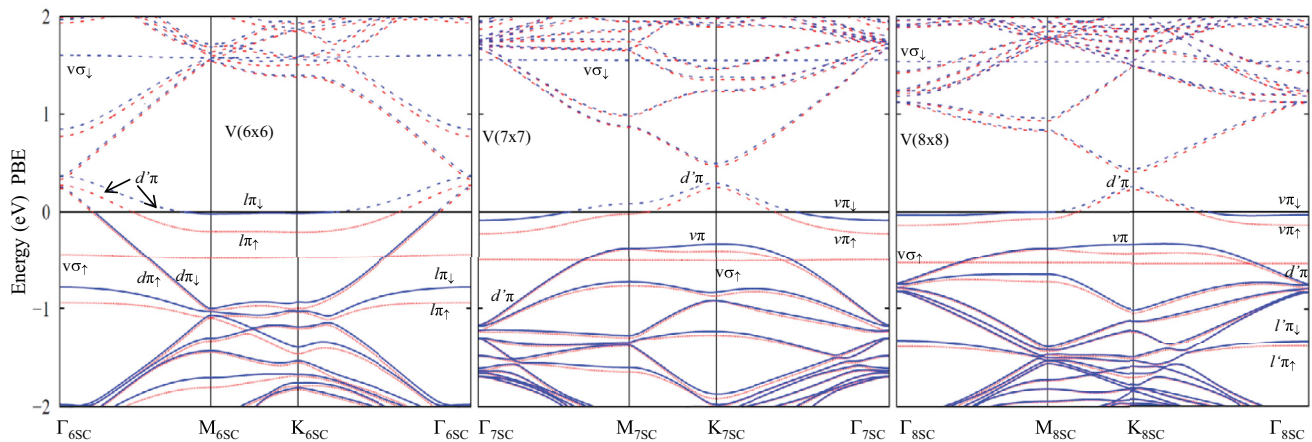


FIG. 4. Band structure for the vacancy defect in the region near the Fermi energy, results from spin-polarized PBE, for the supercells (6×6) at left, (7×7) at center, and (8×8) at right. Solid (dotted) lines indicate occupied (unoccupied) states. Energies aligned to the Fermi energy of the perfect crystal by the $C-1s^2$ average energy.

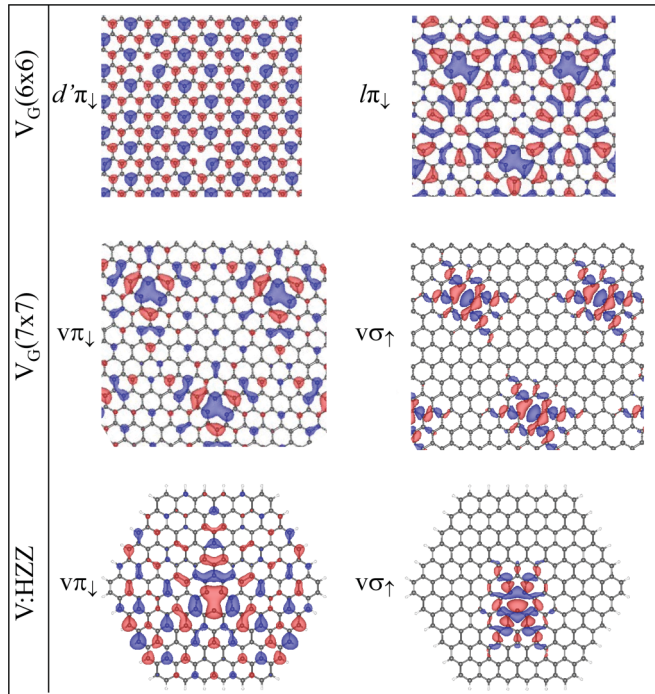


FIG. 5. Isosurfaces for the $d'\pi$, $l\pi$, and $V\pi$ defect states (indicated in Figs. 4 and 6) obtained with the spin-polarized PBE functional; isosurfaces for periodic structures at the Γ point. The $V\sigma$ state shown here for the (7×7) SC and the HZZ cluster presents very similar character in all simulations, and the $l\pi$ state is similar in the (8×8) SC.

value of the magnetic moment can be understood through the energy spectra in Fig. 6: the defect states with different localized character are clearly identified, the lowest-energy occupied defect state $V\sigma$ has higher localization, shows a spin-splitting of ~ 2.0 eV already at the PBE level of theory, and contributes $1\mu_B$ to the magnetization. We can see from Fig. 5 that we recover here the defect state $V\pi$, very similar to that seen in the (7×7) SC. It is more spread over the cluster, the occupied spin orbital is the frontier HOMO level, and the spin-splitting is much lower ~ 0.2 eV than for the $V\sigma$ states. Even so, the $V\pi$ contribution is the same, and for the hexagonal clusters the final magnetic moment is $2\mu_B$.

At this point, we have conflicting results coming from the simulation of the same defect with the same formalism, just different theoretical models: from clusters we obtain $\mu_V = 2\mu_B$ and for the SCs, as seen here and in the extensive literature mentioned above, PBE-sp results give a noninteger magnetic moment, where the spin splitting is complete for the localized σ defect band, but a delocalized defect-induced π -band crosses the Fermi energy.

We now go to the final step of this work, which regards the effect of inclusion of Hartree-Fock exchange in the DFT functional.

In the case of clusters the actual value of μ_V does not change $\mu_V = 2\mu_B$. We see in Fig. 6 a stronger spin-splitting for the defect levels, that for the $V\pi$ state goes from ~ 0.2 to ~ 1.2 eV, and the main impact is in the placing of the acceptor level. The isosurfaces for these specific states in the HZZ cluster are shown in Fig. 5 where we can see the distinct localization

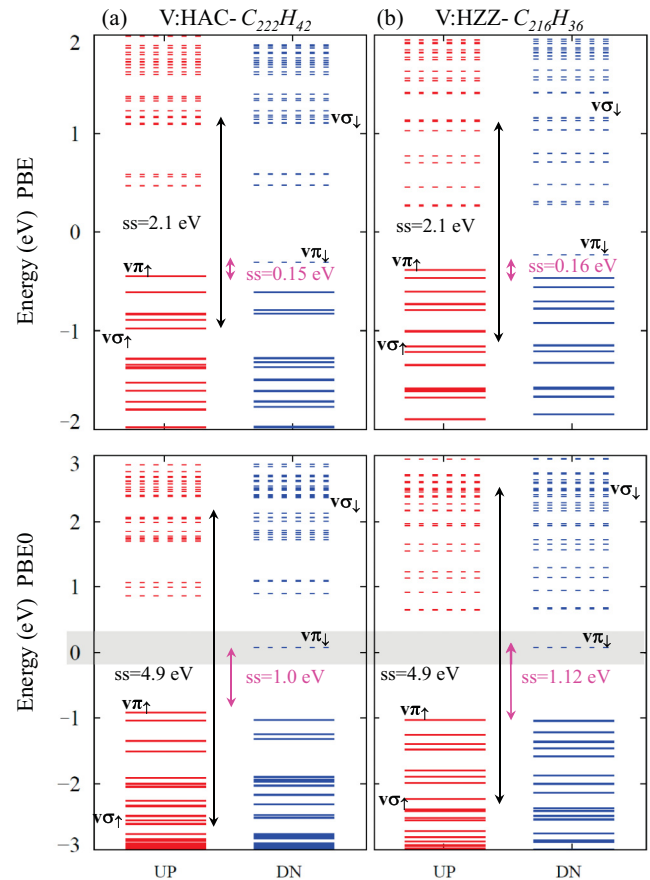


FIG. 6. Electronic energy levels for the vacancy in the clusters HAC- $C_{222}H_{42}$ (left) and HZZ- $C_{216}H_{36}$ (right), in the region near the Fermi energy. Results from spin-polarized PBE (top) and PBE0 (down) functionals. Solid (dotted) lines indicate occupied (unoccupied) states. Energies aligned to the Fermi energy of the perfect crystal by the C- $1s^2$ average energy.

character of the σ and π states (similar characteristics are found for the HAC cluster). We here remark that using the PBE0 α fraction we observe, for all analyzed clusters including the smaller ones, that the vacancy defect state $V\pi$ indicated in Fig. 6 is pinned at $E_F = 0$, as seen by Ugeda *et al.* [3] and in accordance with previous theoretical predictions [6,55], which is not the case using PBE. We pass next to the effect with more impact, seen for all SCs and shown in Fig. 7: We find that the inclusion of the Hartree-Fock exchange eliminates the band-crossing at the Fermi energy in all supercells, enhancing the spin-splitting for the involved states and restoring the vacancy magnetic moment $\mu_V = 2\mu_B$.

Even if the magnetic moment is now the same found for the clusters, defect-defect interaction is still seen by the band anticrossing structure and should not be neglected, and the cell symmetry impacts the defect eigenstate densities. However, another important result coming from the inclusion of the HF exchange comes from the improved character of these eigenstates: We can see that, from the PBE to PBE0 band structure, the width of the $V\pi$ acceptor band decays by ~ 55 – 60% , indicating increased localization, as expected from the mitigation of the self-interaction error [27]. We

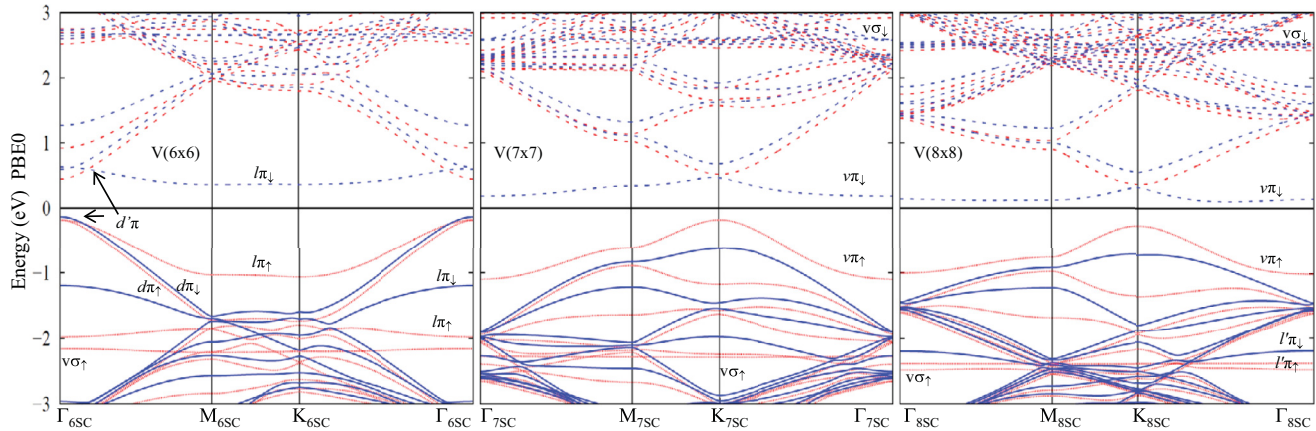


FIG. 7. Band structure for the vacancy defect in the region near the Fermi energy, results from spin-polarized PBE0 for the supercells (6×6) at left, (7×7) at center, and (8×8) at right. Solid (dotted) lines indicate occupied (unoccupied) states. Energies aligned to the Fermi energy of the perfect crystal by the $C-1s^2$ average energy.

note that the acceptor $V\pi_{\uparrow}$ and donor $V\pi_{\downarrow}$ levels show a different localization character (band curvature close to the K_{SC} point) as detected in experimental results [5], and finally that increasing the defect-defect distance from the (7×7) to the (8×8) SC both levels approach the Fermi energy.

Careful analysis of our results, from cluster and periodic boundary conditions and with the inclusion of HF exchange, leads us to predict an integer magnetic moment of $\mu_V = 2\mu_B$ for the isolated vacancy defect. The characteristic $V\sigma$ level, seen in different DFT studies, shows a large spin splitting of very similar magnitude in our different simulations. For the defect π states, we also see a characteristic acceptor level in the cluster and supercells, pinned to the Fermi energy, responsible for the final integer magnetic moment. The confinement effect in the cluster models places the donor level much below, however, from periodic conditions, in the $(3n \pm 1)$ cells, we see this level approaching the Fermi energy.

We turn now to the specific results obtained for the (6×6) SC: the plot in Fig. 8, showing the *spin density* across the cell, highlights the delocalized effect of this $3n$ -array of defects compared to the immediately one-unit larger (7×7) SC. The high spin-density centered on the vacancy site comes from the difference in density between the $l\pi$ up and down states, while the overall delocalization comes from the mixed $d' \leftrightarrow l$ character. We show also the spin density found for the (6×9) SC, where we still see the same density along the zigzag direction in the shorter distance, while along the larger defect-defect distance, which has no parity connection, the density is much lower. We suggest this symmetry-derived behavior could be explored by designing chosen arrays of point defects.

IV. SUMMARY AND CONCLUSION

In summary, we study the vacancy defect in graphene through different approaches, and analyze the effects on the obtained electronic and magnetic structure. We use both cluster and periodic supercell models, and different exchange-correlation functionals, PBE and hybrid DFT-HF, this last with a fraction of Hartree-Fock exchange α chosen to properly describe the electronic properties of graphene close to the

Fermi energy, specifically PBE0 $\alpha = 0.25$. The results from the different simulation models show that, due to the specific symmetry and bilattice properties of graphene, symmetry-related coupling effects have to be carefully probed when using periodic boundary conditions to describe the isolated defect.

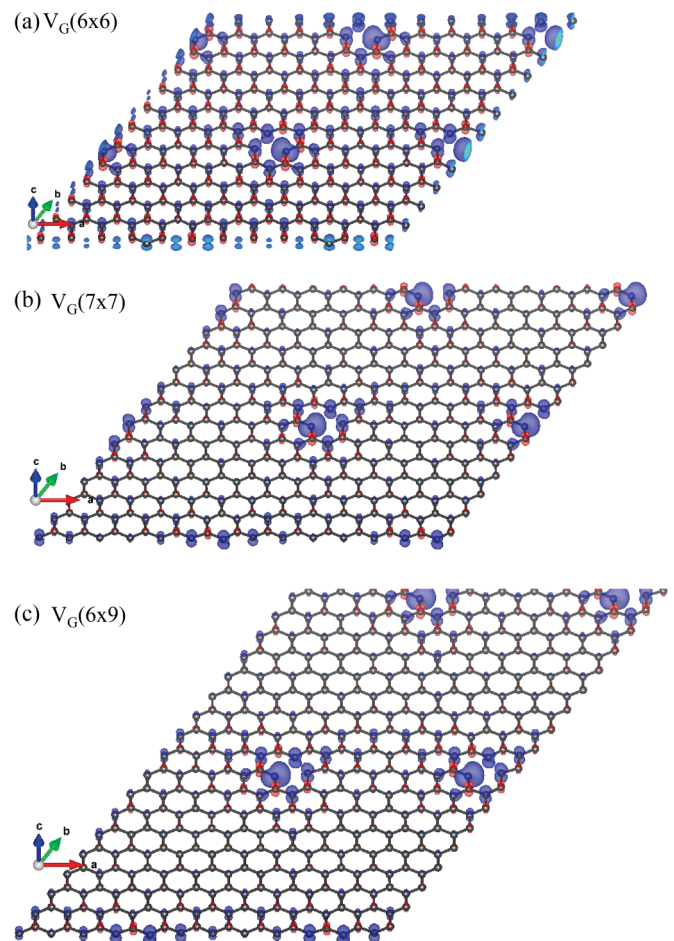


FIG. 8. Isosurfaces for the spin density (0.05\AA^{-3}) produced by the array of vacancies in graphene obtained through PBE0 for (a) 6×6 , (b) 7×7 , and (c) 6×9 SCs.

Our main conclusions are that, even with the extreme rupture of the π bands brought by a vacancy, the delocalization intrinsic to the π states of graphene introduces long-range effects that must be taken into account when analyzing the supercell modeling results; we find also that the inclusion of the proper fraction of Hartree-Fock exchange is crucial for the description of the system, and allows us to arrive at the value of $\mu_V = 2\mu_B$ for the magnetic moment of the isolated vacancy defect, after careful analysis of all adopted models. In addition, we propose that the spin density created by an array of vacancies can show interesting directional properties.

ACKNOWLEDGMENTS

This work was supported by Brazilian agencies FAPESP and CAPES, as well as Brazilian Ministry of Science and Technology grant INEO, and Chilean agency CONICYT; we acknowledge computer time provided by the Center for Research Computing (Rice University) and Superintendência de Tecnologia da Informação (Universidade de São Paulo), and Research Support Center for Nanotechnology and Nanosciences NAP-NN (Universidade de São Paulo). M.J.C. acknowledges support from CNR-S3, Italy. We thank the referees for the comments and fruitful discussions. We thank T. J. D. da Silva, E. Molinari and L. G. Dias da Silva for fruitful discussions.

-
- [1] A. Hashimoto, K. Suenaga, A. Gloter, K. Urita, and S. Iijima, *Nature (London)* **430**, 870 (2004).
- [2] J. C. Meyer, A. K. Geim, M. I. Katsnelson, K. S. Novoselov, T. J. Booth, and S. Roth, *Nature (London)* **446**, 60 (2007).
- [3] M. M. Ugeda, I. Brihuega, F. Guinea, and J. M. Gómez-Rodríguez, *Phys. Rev. Lett.* **104**, 096804 (2010).
- [4] A. W. Robertson, B. Montanari, K. He, C. S. Allen, Y. A. Wu, N. M. Harrison, A. I. Kirkland, and J. H. Warner, *ACS Nano* **7**, 4495 (2013).
- [5] Y. Zhang, S.-Y. Li, H. Huang, W.-T. Li, J.-B. Qiao, W.-X. Wang, L.-J. Yin, K.-K. Bai, W. Duan, and L. He, *Phys. Rev. Lett.* **117**, 166801 (2016).
- [6] V. M. Pereira, F. Guinea, J. M. B. Lopes dos Santos, N. M. R. Peres, and A. H. Castro Neto, *Phys. Rev. Lett.* **96**, 036801 (2006).
- [7] V. G. Miranda, L. G. G. V. Dias da Silva, and C. H. Lewenkopf, *Phys. Rev. B* **94**, 075114 (2016).
- [8] A. A. El-Barbary, R. H. Telling, C. P. Ewels, M. I. Heggie, and P. R. Briddon, *Phys. Rev. B* **68**, 144107 (2003).
- [9] P. O. Lehtinen, A. S. Foster, Y. Ma, A. V. Krasheninnikov, and R. M. Nieminen, *Phys. Rev. Lett.* **93**, 187202 (2004).
- [10] Y. Ma, P. O. Lehtinen, A. S. Foster, and R. M. Nieminen, *New J. Phys.* **6**, 68 (2004).
- [11] O. V. Yazyev and L. Helm, *Phys. Rev. B* **75**, 125408 (2007).
- [12] J. J. Palacios and F. Ynduráin, *Phys. Rev. B* **85**, 245443 (2012).
- [13] M. Casartelli, S. Casolo, G. F. Tantardini, and R. Martinazzo, *Phys. Rev. B* **88**, 195424 (2013).
- [14] C.-K. Lin, *J. Phys. Chem. C* **119**, 27131 (2015).
- [15] M. G. Menezes and R. B. Capaz, *J. Phys.: Condens. Matter* **27**, 335302 (2015).
- [16] L. Rodrigo, P. Pou, and R. Pérez, *Carbon* **103**, 200 (2016).
- [17] H. Padmanabhan and B. R. K. Nanda, *Phys. Rev. B* **93**, 165403 (2016).
- [18] M. D. Petrović and F. M. Peeters, *Phys. Rev. B* **94**, 235413 (2016).
- [19] J. Fernández-Rossier and J. J. Palacios, *Phys. Rev. Lett.* **99**, 177204 (2007).
- [20] W. L. Wang, S. Meng, and E. Kaxiras, *Nano Lett.* **8**, 241 (2008).
- [21] J. M. García-Lastra, *Phys. Rev. B* **82**, 235418 (2010).
- [22] E. H. Lieb, *Phys. Rev. Lett.* **62**, 1201 (1989).
- [23] F. Aikebaier, A. Pertsova, and C. M. Canali, *Phys. Rev. B* **92**, 155420 (2015).
- [24] J. Ding, Z. Qiao, W. Feng, Y. Yao, and Q. Niu, *Phys. Rev. B* **84**, 195444 (2011).
- [25] J. P. Perdew, K. Burke, and M. Ernzerhof, *Phys. Rev. Lett.* **77**, 3865 (1996).
- [26] J. P. Perdew, M. Ernzerhof, and K. Burke, *J. Chem. Phys.* **105**, 9982 (1996).
- [27] M. Pinheiro, M. J. Caldas, P. Rinke, V. Blum, and M. Scheffler, *Phys. Rev. B* **92**, 195134 (2015).
- [28] S. Just, S. Zimmermann, V. Kataev, B. Büchner, M. Pratzer, and M. Morgenstern, *Phys. Rev. B* **90**, 125449 (2014).
- [29] M. V. Ulybyshev and M. I. Katsnelson, *Phys. Rev. Lett.* **114**, 246801 (2015).
- [30] V. Blum, R. Gehrke, F. Hanke, P. Havu, V. Havu, X. Ren, K. Reuter, and M. Scheffler, *Comput. Phys. Commun.* **180**, 2175 (2009).
- [31] A. Tkatchenko and M. Scheffler, *Phys. Rev. Lett.* **102**, 073005 (2009).
- [32] V. Havu, V. Blum, P. Havu, and M. Scheffler, *J. Comp. Phys.* **228**, 8367 (2009).
- [33] H. J. Monkhorst and J. D. Pack, *Phys. Rev. B* **13**, 5188 (1976).
- [34] A. J. Cohen, P. Mori-Sánchez, and W. Yang, *Science* **321**, 792 (2008).
- [35] S. Kümmel and L. Kronik, *Rev. Mod. Phys.* **80**, 3 (2008).
- [36] C. Adamo and V. Barone, *J. Chem. Phys.* **110**, 6158 (1999).
- [37] P. E. Trevisanutto, C. Giorgetti, L. Reining, M. Ladisa, and V. Olevano, *Phys. Rev. Lett.* **101**, 226405 (2008).
- [38] L. Yang, J. Deslippe, C.-H. Park, M. L. Cohen, and S. G. Louie, *Phys. Rev. Lett.* **103**, 186802 (2009).
- [39] Y.-J. Yu, Y. Zhao, S. Ryu, L. E. Brus, K. S. Kim, and P. Kim, *Nano Lett.* **9**, 3430 (2009).
- [40] C. Cocchi, D. Prezzi, A. Ruini, M. J. Caldas, and E. Molinari, *J. Phys. Chem. A* **118**, 6507 (2014).
- [41] X. Jia, M. Hofmann, V. Meunier, B. G. Sumpter, J. Campos-Delgado, J. M. Romo-Herrera, H. Son, Y.-P. Hsieh, A. Reina, J. Kong, M. Terrones, and M. S. Dresselhaus, *Science* **323**, 1701 (2009).
- [42] C. Cocchi, D. Prezzi, A. Ruini, E. Benassi, M. J. Caldas, S. Corni, and E. Molinari, *J. Phys. Chem. Lett.* **3**, 924 (2012).
- [43] T. Enoki, *Phys. Scr.* **T146**, 014008 (2012).
- [44] S. Fujii and T. Enoki, *Acc. Chem. Res.* **46**, 2202 (2013).
- [45] V. Barone, O. Hod, J. E. Peralta, and G. E. Scuseria, *Acc. Chem. Res.* **44**, 269 (2011).

- [46] P. Puschnig and D. Lüftner, *J. Electron Spectrosc. Relat. Phenom.* **200**, 193 (2015).
- [47] W. L. Wang, O. V. Yazyev, S. Meng, and E. Kaxiras, *Phys. Rev. Lett.* **102**, 157201 (2009).
- [48] R. Singh and P. Kroll, *J. Phys.: Condens. Matter.* **21**, 196002 (2009).
- [49] B. Wang and S. T. Pantelides, *Phys. Rev. B* **86**, 165438 (2012).
- [50] H. A. Jahn and E. Teller, *Proc. R. Soc. London A* **161**, 220 (1937).
- [51] C.-C. Lee, Y. Yamada-Takamura, and T. Ozaki, *Phys. Rev. B* **90**, 014401 (2014).
- [52] A. Krasheninnikov, P. Lehtinen, A. Foster, and R. Nieminen, *Chem. Phys. Lett.* **418**, 132 (2006).
- [53] A. Santana, A. M. Popov, and E. Bichoutskaia, *Chem. Phys. Lett.* **557**, 80 (2013).
- [54] S. T. Skowron, I. V. Lebedeva, A. M. Popov, and E. Bichoutskaia, *Chem. Soc. Rev.* **44**, 3143 (2015).
- [55] V. M. Pereira, J. M. B. Lopes dos Santos, and A. H. Castro Neto, *Phys. Rev. B* **77**, 115109 (2008).
- [56] F. Banhart, J. Kotakoski, and A. V. Krasheninnikov, *ACS Nano* **5**, 26 (2011).
- [57] P. Giannozzi, S. Baroni, N. Bonini, M. Calandra, R. Car, C. Cavazzoni, D. Ceresoli, G. L. Chiarotti, M. Cococcioni, I. Dabo, A. Dal Corso, S. de Gironcoli, S. Fabris, G. Fratesi, R. Gebauer, U. Gerstmann, C. Gougoussis, A. Kokalj, M. Lazzeri, L. Martin-Samos, N. Marzari, F. Mauri, R. Mazzarello, S. Paolini, A. Pasquarello, L. Paulatto, C. Sbraccia, S. Scandolo, G. Sclauzero, A. P. Seitsonen, A. Smogunov, P. Umari, and R. M. Wentzcovitch, *J. Phys.: Condens. Matter.* **21**, 395502 (2009), see also <http://www.quantum-espresso.org>.